ACTIVE WHIRL FLUTTER CONTROL THROUGH DYNAMIC WIND TUNNEL EXPERIMENTS AND MODELLING

Dr. Sam Bull, s.c.bull@bath.ac.uk, The University of Bath (UK)
Mr. Dami Adeyemi, da359@bath.ac.uk, The University of Bath (UK)
Dr. David Cleaver, d.j.cleaver@bath.ac.uk, The University of Bath (UK)
Dr. Jonathan du Bois, jldb20@bath.ac.uk, The University of Bath (UK)

Abstract

Whirl flutter aeroelastic instability is a well-known limiter of performance in current generation tiltrotors, and as such, its study is of particular interest for future rotorcraft generations. This paper presents two integrated systems aiming to facilitate novel analysis of the whirl flutter phenomenon and its alleviation through active mini-tab control: a bespoke experimental rig, and a complementary numerical model. This is the first experimental and numerical investigation of active whirl flutter control with a promising, and practically realisable flow control technology. The experimental rig is shown to be capable of producing dynamic motion comparable to documented XV-15 flutter, while LQR analysis of the reduced-order model suggests the feasibility of linear control, which offers unique advantages over nonlinear control for practical implementation of the technology. A mutually beneficial relationship is established between physical testing and numerical investigation enabling state of the art data collection and analysis.

1. INTRODUCTION

1.1. Motivation

The wing-rotor-nacelle systems found in tiltrotors are susceptible to whirl flutter in forward flight. This condition involves an aeroelastic coupling of the pitching and yawing modes of the nacelle caused by precessional behaviour arising from the aerodynamic loads applied at the proprotor. This coupling is gyroscopic in nature and can compromise tiltrotor operation beyond critical flight speeds. The occurrence of whirl flutter can lead to unstable vibrations and catastrophic damage to the aircraft. This has led to tiltrotors requiring overly thick wings to compensate, increasing drag and structural mass.

Active vibration suppression techniques are an attractive, alternative solution as they can stabilise the response of the wing-rotor-nacelle system through the introduction of controllable aerodynamic loads, augmenting the flutter boundaries and relaxing the wing thickness constraint. Previous numerical work by Hathaway and Gandhi [1] has demonstrated whirl flutter suppression through simulation of active wing flaperon control, increasing the stability boundary by 50 kn. This work seeks to experimentally and numerically assess the efficacy of a small control surface called the mini-tab (flow fence), that protrudes normal to the wing surface, for active whirl flutter control. This has two advantages over wing flaperon control. Firstly, due to the relatively low mass, the mini-tab has a higher bandwidth/faster response times. Secondly, the mini-tab is a separate entity to the main flight control surfaces and thus avoids any saturation issues associated with different trim states in the flight envelope. We envision that such a stand-alone device would be easier to certify.

1.2. Objectives

The objectives of this investigation are:

- Create a validated model of the wing-rotor-nacelle system that can correctly capture whirl flutter boundaries.
- Experimentally characterise the mini-tab performance in wing motions representative of whirl flutter.
- Create a reduced-order mini-tab model for use in numerical active whirl flutter control simulations.
- Validate the aerodynamic load control output from simulations in wind tunnel experiments.

This is the first experimental and numerical investigation of active whirl flutter control with a promising, and practically realisable flow control technology. However, to experimentally study whirl flutter control, a rig capable of replicating the degrees of freedom at representative whirl flutter conditions is required. Such a rig currently does not exist, so a bespoke rig has been designed and built, and will be presented here.

This paper is split into two parts. The first is an overview of the experimental rig design and current progress (Section 2); the second is a summary of the reduced-order modelling of the wing-rotor-nacelle system (Section 3).

Presented at 47th European Rotorcraft Forum, United Kingdom, 7-9th September, 2021

2. EXPERIMENTAL RIG DESIGN

2.1. Dynamic Motion

The design starts from a simplified representation of a tilt rotor wing-rotor-nacelle assembly in whirl flutter, as shown in Figure 1. In this representation, the propeller is connected to a flexible finite wing structure that is fixed at the root. During whirl flutter modes, the wing will deform in three degrees of freedom, namely flap, row, and twist, see Figure 1.

This experimental study considers a 2D representation of this system. If a plane is taken at a spanwise point, the wing deformations can be represented by two rectilinear translations (plunge, surge) and one rotation (pitch). These are the degrees of freedom the experimental rig will replicate.

CAD images of the experimental rig are presented in Figure 2. The rig operates using air bearings that constrain a moving assembly (blue) to the page plane (TOP VIEW) whilst permitting virtually frictionless motion. The air bearings can be seen in

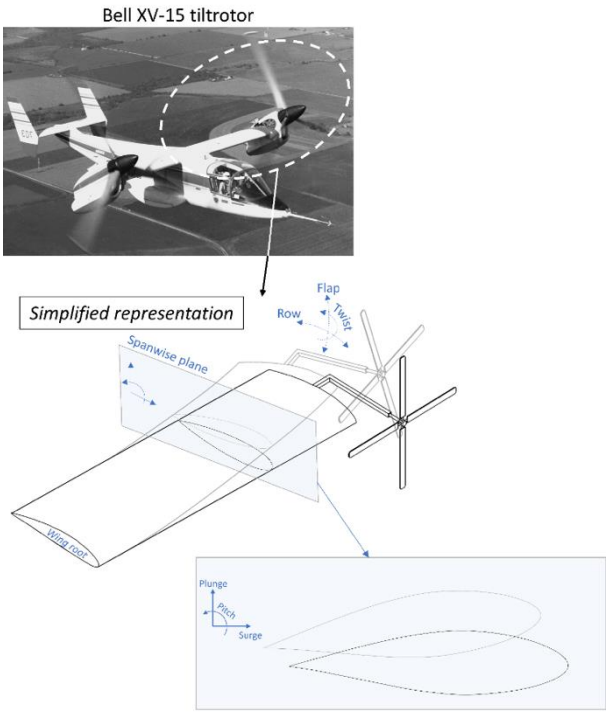

Figure 1: Degrees of freedom for tiltrotor wing/propeller system and representative 2D planar motion.

the SIDE VIEW. They provide pressured air to the underside of the top disc, and the topside of the bottom disc, constraining vertical motion. Three hydraulic servo-actuators (yellow) control the moving assembly in three degrees of freedom; plunge, surge, and pitch (TOP VIEW). The wing is mounted underneath the moving assembly (ISO VIEW), hanging vertically into the wind tunnel test section, spanning from floor to ceiling. An aerofoil overlay can be seen in the TOP VIEW which represents the wing cross-section projected upwards through the moving assembly.

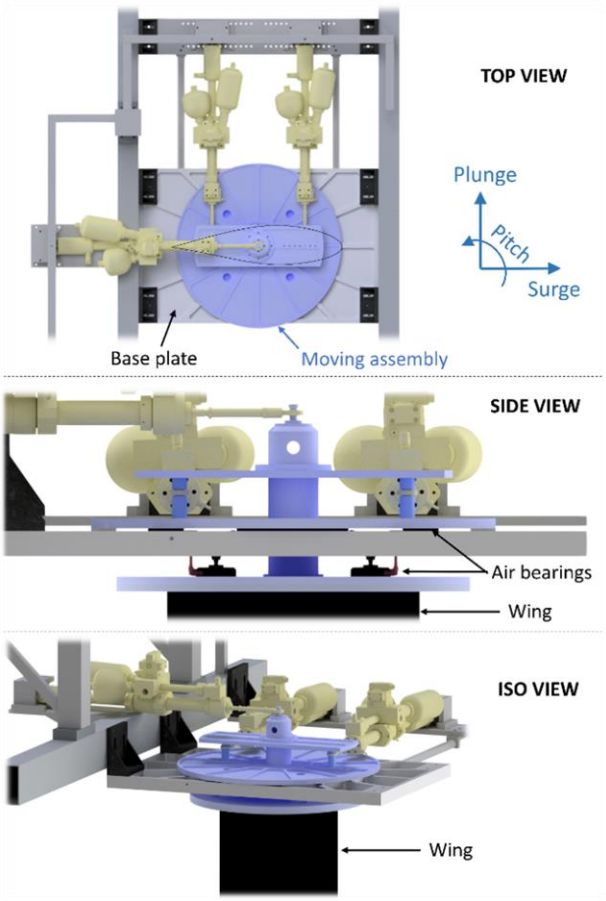

Figure 1: CAD renderings - TOP VIEW: Moving assembly (blue) can be moved in three degrees of freedom by the three servo-actuators (yellow). Rig is situated above the wind tunnel test section and the wing is hung from underneath the moving assembly (SIDE VIEW/ISO VIEW) which is represented by the aerofoil cross-section). SIDE VIEW: Shows the air bearings that constrain the moving assembly to a single plane. ISO VIEW: Wing is hung into the wind tunnel from above.

Each actuator is connected to the moving assembly by a spherical rod end, and supported at the rear by a bespoke universal joint to constrain rolling of the actuators about their piston axis. Required actuator extensions/contractions are calculated from inverse kinematics of the wing plunge, surge, and pitch positions, which are then implemented via closed-loop PI control on the position signal with

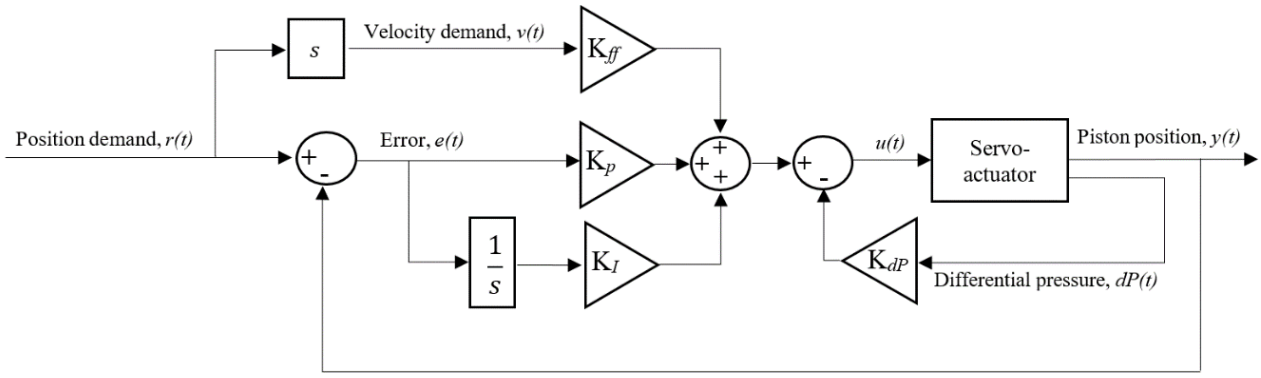

Figure 3: Control structure for servo-hydraulic actuators

velocityfeed-forward and differential cylinder pressure feedback, see Figure 3. This control architecture yields a satisfactory frequency response for both gain and phase, see bode plot in Figure 4. There is a noticeable increase in gain beyond 5 Hz for both pitch (blue) and plunge (black), indicative of a resonant peak of the rig and supporting frame system. This is verified by the surge motion response (red), where input frequency was limited to 5 Hz due to large oscillations observed in the supporting frame and is highlighted by the increased gain in surge (red), see Figure 4. The wind tunnel frame is heavily reinforced in the plunge direction *only* and work currently ongoing to reinforce the frame in the surge direction to push the resonant peak to higher frequencies and broaden the test envelope for surge motions.

To put the bode plot in context of whirl flutter, we consider a 'typical' reduced frequency for the XV-15 aircraft, which is defined as

$$(1)\quad k = \frac{\pi f c}{U_\infty}$$

where k is the reduced frequency, f is the oscillation frequency, c is the chord length of the wing and U_∞ is the free-stream velocity (or flight speed). This represents the ratio of two time scales; the period of wing oscillation during whirl flutter and the time taken for a parcel of fluid travelling at the free-stream velocity to travel a distant of one chord length. This is helpful in designing experiments to replicate full-scale flight conditions, where the models and incoming air velocity will be smaller due to wind tunnel constraints. From the stability margin data of the XV-15 by Acree *et al.* [2], we estimate whirl flutter to occur between $k = 0.10$ to 0.25.

To define the oscillation frequency of the experiments the Reynolds number is required, which is defined as

$$(2)\quad Re = \frac{\rho U_\infty c}{\mu}$$

where ρ and μ are the fluid's density and dynamic viscosity respectively. The Reynolds number for the XV-15 in forward flight sits within a range of 10 to 20 million, which is extremely difficult to achieve in wind tunnel testing due to constraints on the model size (chord length, c) and the free-steam velocity, U_∞. It can also be seen from (1) and (2) that a higher Reynolds number (assuming a constant chord length) requires a higher oscillation frequency, f to achieve a certain reduced frequency, k, which is also subject to experimental constraints (i.e., hydraulic performance, structural vibrations). As we are concerned with unsteady aerodynamics in this study, we favour a lower Reynolds number of 1,000,000 to give better hydraulic performance and reduced structural deformations. A chord length of 0.5 m was identified from the wind tunnel geometry (shown in the next section), which requires a free-stream velocity of 30 m/s to achieve a Reynolds number of 1,000,000. The maximum experimental frequency of oscillation can then be found from (1) to be

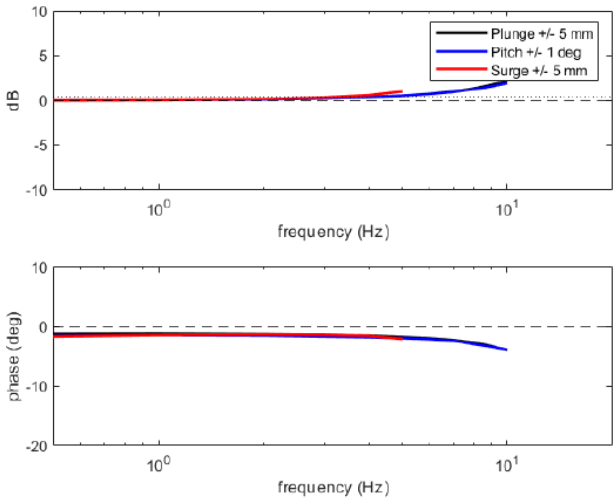

Figure 4: Bode plot of rig performance

approximately 5 Hz at k = 0.25, which sits within the acceptable range of the bode plot (Figure 4).

2.2. Wing Design

The experimental wing is based on the XV-15 profile, which uses a NACA 64A-223 section. This not only provides a representative geometry to demonstrate active control, but the 26% thick section also provides a large internal volume for instrumentation, i.e., pressure sensors, mini-tabs, motors, drives, accelerometers, and cables. As stated in the previous section, the experiment is 2D, meaning the wing must minimise any spanwise variations in flow and mitigate wing tip effects. This is achieved by allowing the wing to span the full height of the wind tunnel test section (ceiling to floor), see Figure 5, with a 15 mm (3% c) gap between the wing tip and tunnel floor to accommodate wing motion/deflection. A chord length of 0.5 m spanning the full height of 1.5 m yields a 2D aspect ratio of 3, which was deemed a satisfactory compromise between tunnel wall effects and wing structure/internal volume (as an increase in aspect ratio demands a reduction in chord length).

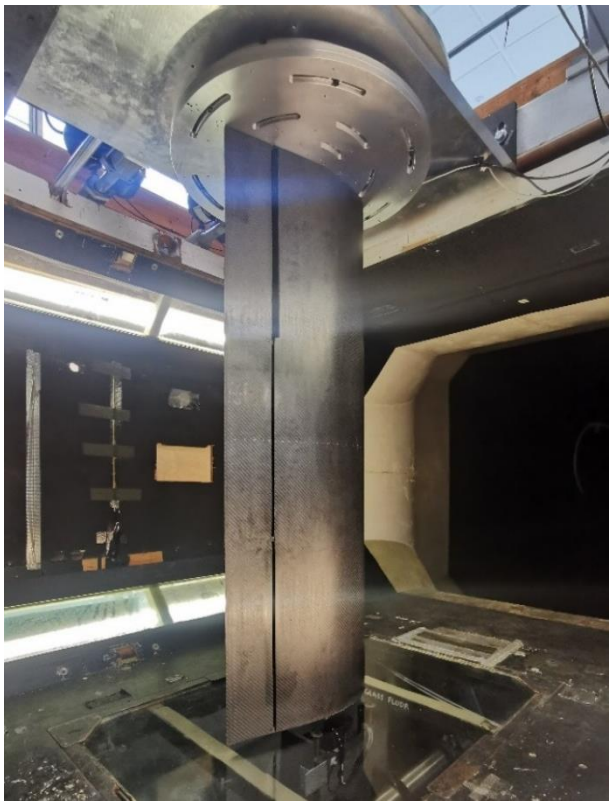

Figure 5: Wing in-situ

An example of the envisioned mini-tab wing placement is shown in Figure 6. Here the mini-tab extends along a short segment of the span, at some distance from the wing root. Once again, this is projected onto a spanwise plane to produce a 2D representation. The aerodynamic effects are as follows: when the mini-tab extends into the upper surface flow, the lift is reduced and the pitching moment is increased, and vice versa when the mini-tab extends into the lower surface flow [3]. Note that due to the 2D representation, any spanwise variations or propeller wake effects will be neglected. To implement the mini-tab geometry it was necessary to build the wing in two distinct sections. This can be seen in Figure 7a, where the mini-tab splits the carbon composite wing structure towards the trailing edge. A link between the two sections is provided by four equally spaced ribs along the span and as a consequence, the mini-tab needed to be split into three equal assemblies with a small gap (4% c) between them to accommodate the supporting ribs.

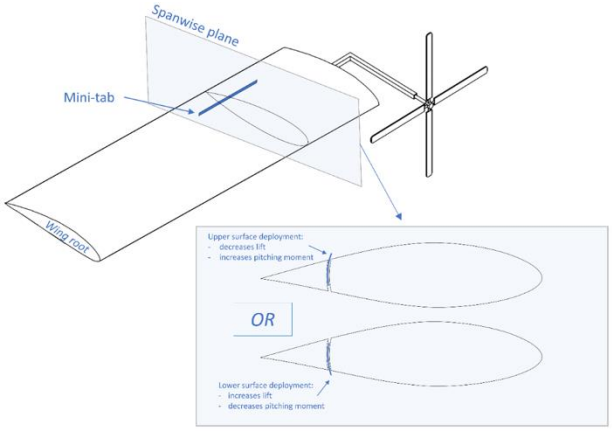

Figure 6: Representation of wing mini-tab placement and mini-tab deployment.

A simple rotation deployment mechanism was implemented for this experiment, shown in Figure 7b, which is driven by an EC60 brushless Maxon motor. Tab deployment heights from the upper and lower surface can reach up to 4% c (Figure 7c). Force, moment and unsteady surface pressure measurements will be obtained at the mid-span plane through 42 ±60 mbar Honeywell TruStability HSC PCB mounted pressure transducers with an I2C digital interface (Figure 7d), which can be logged at a rate of 2000 Hz. Internal tubing length has been kept to a minimum (<60 mm) for the pressure source - transducer connection. This tubing length has been deemed acceptable by measuring the frequency response to a periodic pressure source [4].

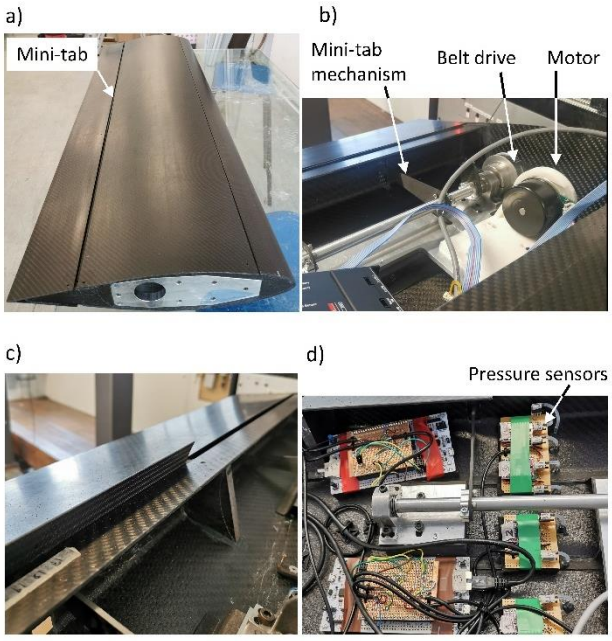

Figure 7: a) Full wing assembly, b) Mini-tab mechanisms and motor, c) Close-up of mini-tab max. deployment height, d) in-house pressure measurement system.

2.3. Experiments: Future work

Once full commissioning of the rig for unsteady wing motion and mini-tab testing is complete, a test campaign will be conducted to address the following:

- **Unsteady aerodynamic characterisation of airfoil:** A cheap and accurate unsteady aerodynamics model is required for the numerical whirl flutter simulations (shown in the next section). Reduced-order models exist for unsteady aerodynamics in pitch, plunge [5] and surge [6]. However, the validity of these models for a 26% thick airfoil may come into question. If required, a data-driven approach for reduced-order modelling can be taken, as demonstrated in [7].
- **Mini-tab characterisation:** This will be conducted in three stages. The first will determine the quasi-steady lift, drag and pitching moment changes vs. deployment height at different angles of attack. The second will determine the transient response of rapid mini-tab deployment. Previous work [3] has shown the transient response can be approximated by a first-order system. Finally, the effect of unsteady wing motion on mini-tab performance will be determined.

3. NUMERICAL WHIRL FLUTTER MODELLING

The experimental work outlined here is complemented by numerical modelling of the relevant whirl flutter dynamics in MATLAB and Simulink. While current multibody analysis tools like CAMRAD II [8] and Dymore [9] can produce high-fidelity whirl flutter predictions, they have a high computational requirement which is less well suited to control development needs, where high speed computations are needed for practical development purposes. For this reason, priority is given to simpler, low-order, linear approaches.

3.1. Base System and Model Description

The base model describes the Bell XV-15 research aircraft [10] and is developed according to the experimentally validated methodology formulated in [11] for a 3-bladed, gimballed rotor of radius R spinning at frequency Ω in windmilling configuration, close to the dynamic conditions experienced in cruise. The windmilling assumption implies that a virtual engine instantaneously supplies whatever torque is required to maintain a constant rotor speed during any perturbed motion. Prior to excitation, the rotor is assumed to be operating in pure axial flow, with freestream velocity, V, which may be written as a dimensionless advance ratio ($V/\Omega R$).

The wing-rotor-pylon system is treated in isolation as a semi-span structure and assumed to be cantilevered at the root. Structural dynamics of the wing are included initially through modal methods wherein mode shapes are assumed for the primary bending modes of the wing. Higher frequency vibration modes are excluded due to their relatively low participation in the flutter mechanism. Outstanding properties of the wing relating to inertia, stiffness and damping are also incorporated from [11]. The motion of the structure is captured through nine degrees of freedom, three of which are associated with wing displacement including plunge (q_1), surge (q_2) and torsion (p). The remaining six are associated with rotor displacement including collective flap/lag relative to the rotor hub (β_0, ζ_0); cyclic flap about the rotor gimbal (β_{1C}, β_{1S}); and shifts in the coordinates of the rotor center of gravity due to cyclic lagging of the rotor blades during rotation (ζ_{1C}, ζ_{1S}). Figure 8 summarises the structure. Note that, q_1 and q_2 are normalised states defined by x_P/L_w and z_P/L_w respectively, where L_w is the XV-15 wing semispan. The torsion state p is equal to α_y.

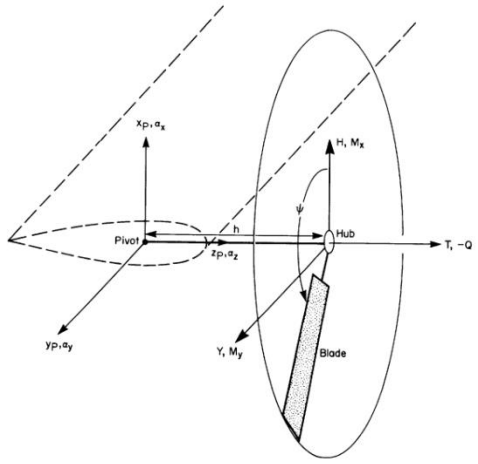

Figure 8: Wing Rotor System modified from [11]

Wing and rotor aerodynamics are accounted for on a quasi-steady basis as is common for this type of aeroelastic analysis [12-14]. Aerodynamics are first evaluated for a general 2-dimensional cross-section of the wing/rotor blade, before being integrated across their respective spans to obtain the aerodynamic loading. The full aerodynamic characterisation features 24 integrals describing contributions of the wing/rotor motion and the freestream to aerodynamic loads across the subsystem.

3.1.1. Stability Analysis

The result of the above modelling is a system of linear equations that are readily treated by classical linear stability analysis tools. The general form of these equations is

$$\boldsymbol{M}\ddot{x} + \boldsymbol{G}\dot{x} + \boldsymbol{K}x = 0 \tag{3}$$

where $\boldsymbol{M}, \boldsymbol{G}$ and $\boldsymbol{K}$ are the mass, damping and stiffness matrices respectively, and x is a vector containing all rotor and wing states. These equations of motion can be written in state space form as

$$\dot{q} = \boldsymbol{A}q + \boldsymbol{B}u \tag{4}$$

where

$$\boldsymbol{A} = \begin{bmatrix} [0] & [I] \\ -M^{-1}K & -M^{-1}G \end{bmatrix}, \qquad q = \begin{bmatrix} x \\ \dot{x} \end{bmatrix}, \qquad q = \begin{bmatrix} \dot{x} \\ \ddot{x} \end{bmatrix}$$

An eigen analysis of the system matrix $\boldsymbol{A}$ yields eigenvector/eigenvalue pairings containing: (i) mode shape information and (ii) the frequency (ω_n) and damping (ζ_n) properties of the dynamic system respectively. For a particular eigenvalue (λ_n):

$$\omega_n = Im(\lambda_n) \tag{5}$$

$$\zeta_n = \frac{Re(\lambda_n)}{\sqrt{Im(\lambda_n)^2 + Re(\lambda_n)^2}} \tag{6}$$

The critical flutter speed is that at which the system transitions from stable to unstable, at the point where the damping ratio is zero ($\zeta_n = 0$).

3.1.2. Model Validation

To ensure a faithful reproduction of Johnson's model, outputs of the computational MATLAB model are compared with the results presented in [11]. Table 1 shows a summary of the key XV-15 parameters in Johnson's original nomenclature.

XV-15 parameter		Symbol	Value	Units
Configuration properties				
Number of blades		N	3	~
Rotor radius		R	3.82	m
Rotor speed		Ω	48	$rad\ s^{-1}$
Lock number		γ	3.83	~
Solidity		σ	0.089	~
Blade lift curve slope		α	5.7	~
Advance Ratio		$V/\Omega R$	0.7	~
Rotor shaft length		h	1.3	m
Inertial properties				
Blade Inertia		I_b	142	$kg\ m^2$
Blade Flapping Inertia	Cyclic	I_β	142	$kg\ m^2$
	Collective	$I_{\beta 0}$	111	$kg\ m^2$
Blade Lag Inertia	Cyclic	I_ζ	95	$kg\ m^2$
	Collective	$I_{\zeta 0}$	142	$kg\ m^2$
stiffness and damping properties				
Plunge stiffness		K_{q1}	9.20E+06	$kg\ m^2/s^2$
Surge stiffness		K_{q2}	2.50E+07	$kg\ m^2/s^2$
Torsional stiffness		K_p	1.77E+06	$kg\ m^2/s^2$
Plunge damping ratio		C_{q1}	9.03E+03	$kg\ m^2/s$
Surge damping ratio		C_{q2}	2.73E+04	$kg\ m^2/s$
Torsional damping ratio		C_p	9.60E+02	$kg\ m^2/s$

Table 1: XV-15 Key Model Parameters

Results are presented in Figures 9 and 10 for modal frequency (per rev) and damping ratio (%) variation with advance ratio for $0 \leq V/\Omega R \leq 1.6$. Of the available vibration outputs, data for eight modes are presented. The first three relate to the primary (low frequency, non-rigid) wing bending modes: the wing plunge mode q_1; the wing surge mode q_2; and the wing torsion mode p, while the remaining five are associated with the eigen analysis of the rotor equations of motion: the collective flap mode β_0; the low frequency flap mode (β-1); the low frequency lag mode (ζ-1); the high frequency flap mode (β+1); and the high frequency lag mode (ζ+1).

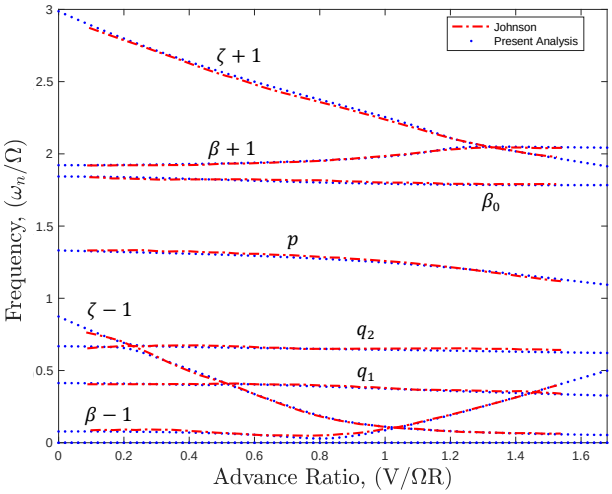

Figure 9: Model Validation: Modal Frequency

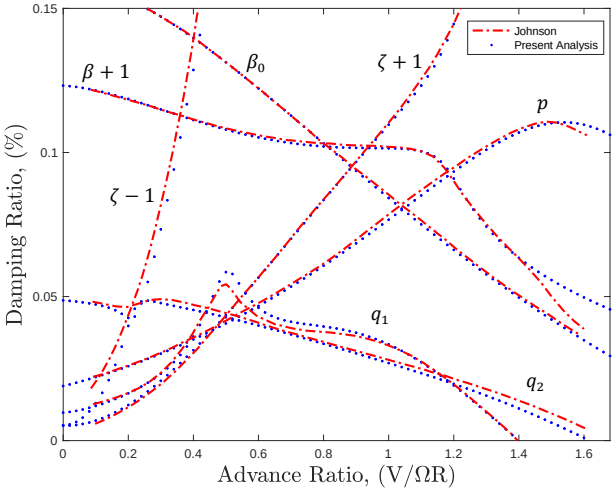

Figure 10: Model Validation: Modal Damping Ratio

A comparison of both cases shows that the MATLAB model provides good tracking across the entire advance ratio sweep. Frequency data in particular shows excellent agreement, and despite some differences visible in Figure 10, damping in the MATLAB reproduction is assessed to be a good fit to the experimental data presented in [11].

3.2. Model Adaptations

3.2.1. Wing Model Modifications

To permit the introduction of flow control devices at finite locations along the wing, the modal representation of the wing is replaced with an Euler-Bernoulli finite element (FE) model. As a result, the number of wing degrees of freedom is increased from 3 to $5(n+1)$ for a wing modelled with n beam elements. The discrete state vector for a FE beam element is:

$$q_w = [x_1\ z_1\ \theta_1\ \psi_1\ \phi_1\ x_2\ z_2\ \theta_2\ \psi_2\ \phi_2]^T$$

The x_n and z_n states are the plunge and surge displacements, and the θ_n, ψ_n and ϕ_n states are rotations in pitch, yaw, and roll. Note that the state describing the spanwise wing extension remains excluded from the analysis due to low participation in the relevant dynamics. Subscripts 1 and 2 indicate degrees of freedom at the two nodes of the beam element. Discrete states are related to continuous wing states so that:

$$u_w = [H]q_w \tag{7}$$

For:

$$[H] = \begin{bmatrix} H_b^1 & 0 & 0 & 0 & H_b^2 & H_b^3 & 0 & 0 & 0 & H_b^4 \\ 0 & H_b^1 & 0 & H_b^2 & 0 & 0 & H_b^3 & 0 & H_b^4 & 0 \\ 0 & 0 & H_\theta^1 & 0 & 0 & 0 & 0 & H_\theta^2 & 0 & 0 \end{bmatrix}$$

The shape function matrix $[H]$ contains standard cubic polynomial shape functions for a beam undergoing vertical and horizontal deformation $(H_b^1, H_b^2, H_b^3, H_b^4)$ in addition to torsional deformation (H_θ^1, H_θ^2). Formal definitions of these shape functions may be found in [15].

For a beam element of length l, the continuous form of the wing structural stiffness matrix $[K_w]$ is then obtained through linear beam theory to give:

$$[K_w] = \int_0^l \frac{d^2[H]^T}{dl^2} \begin{bmatrix} EI_x & 0 & 0 \\ 0 & EI_z & 0 \\ 0 & 0 & GJ_\theta \end{bmatrix} \frac{d^2[H]}{dl^2} \tag{8}$$

The flexural rigidities in plunge (EI_x), surge (EI_z) and torsion (GJ_θ) can then be tuned so that the primary wing bending frequencies match those presented in Figure 9.

3.2.1. Mach Number Corrections

Although Johnson does mention Glauert-Prandtl corrections for Mach Number/compressibility effects in his NASA report, the validation results presented in Figures 9 and 10 for the base model do not make use of them. These corrections are included in the rotor model at this juncture by modifying the blade section lift curve slope so that:

(9) $$c_{l_\alpha} = c_{l_\alpha} \frac{1}{\sqrt{1-M^2}}$$

Where M is the localised Mach Number for a blade section, determined by the rotor speed Ω and the section distance r from the blade root. The localised Mach Number can be expressed as it relates to the blade tip Mach Number M_{tip}, and the inflow velocity V:

(10) $$M = M_{tip}\sqrt{(\Omega r)^2 + V^2}$$

Finally, the localised blade section Mach Number is truncated to its value at 0.95 for $M > 0.95$ to avoid singularities induced by Equation 9 at $M = 1$.

3.2.2. Mini-tab Modelling

Aerodynamic loading of the mini-tab is currently included through experimental data collected at the University of Bath [16]. The configuration simulated here is a trailing edge mini-tab centralised about the midspan of the wing. The mini-tab has length, $L_{mt}/L_w = 0.5$, with chordwise location $x_{mt}/c = 0.95$ (positive aft of the leading edge) and maximum tab extension, $h_{mt}/c = \pm 0.04$. Mini-tab properties are normalised by chord length c or wing semispan L_w to facilitate scaling with changes in the structural wing model. Positive mini-tab extension implies deployment on the upper surface of the wing while negative tab extension implies deployment at the same position on the lower surface. Note that there is a positive drag penalty associated with tab deployment on both the upper and lower surfaces, leading to a nonlinear discontinuity that will be discussed in more depth later.

Characterisation experiments conducted in [16] showed that a power law was a good approximation to the mini-tab loading behaviour, so power law curves were fit to the available mini-tab data. An example of the fitting process is provided in Figure 11. The data used in [16] covers induced changes in lift (ΔC_l) for 40 angles of attack (α) in the range: $-20° \leq \alpha \leq 20°$. Although sufficient data is available for mini-tab lift variation, data is limited for the induced pitching moment and drag with respect to angle of attack and h/c. To address this limitation, it is assumed that the lift, drag and pitching moments scale in proportion to each other with variation in h/c. This relationship is represented by an amplitude ratio AR where

(11) $$AR = \frac{\Delta C_l}{\Delta C_{l_{MAX}}} = \frac{\Delta C_m}{\Delta C_{m_{MAX}}} = \frac{\Delta C_d}{\Delta C_{d_{MAX}}}$$

The 'max' subscripts used here denote force/moment deltas at maximum tab extension ($h/c = 0.04$).

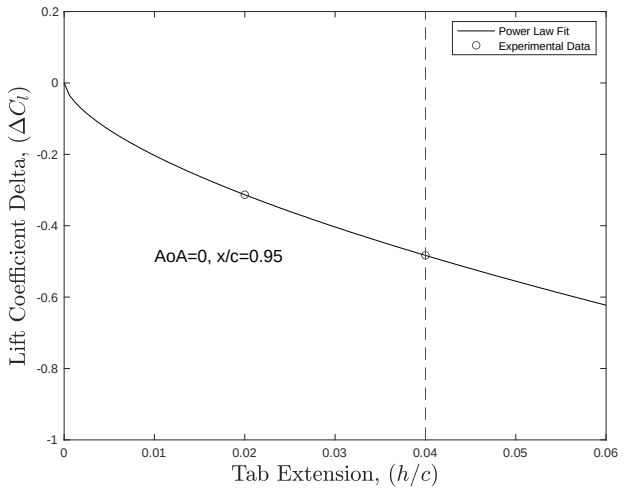

Figure 11: Power law fit to mini-tab data (α = 0, x/c=0.95)

3.3. LQR Control

Mini-tab control on the simulated system will be implemented using linear quadratic Gaussian (LQG) control, comprised of a full-state feedback linear quadratic regulator (LQR) with Kalman filter estimation of any unobserved system states. LQR produces an optimal solution, $u = -Kx$, for linear stability through minimisation of the quadratic cost function:

(12) $$J = \int_0^\infty (x^T[Q]x + u^T[R]u)\, dt$$

Matrices $[Q]$ and $[R]$ define the weighting of the control with respect to the tracked system state(s) and the control input respectively. They are tuned to maximise the increase in the critical flutter velocity while ensuring that tab extensions and frequency limits remain realistic.

Given that the LQR is a linear controller, nonlinearities from the power law inclusion in the mini-tab modelling must be linearised to accommodate implementation. The drag experiences a discontinuous gradient at the trim state, so the linear model neglects the drag force. The controller may then be tuned for a linear system by linearising the mini-tab model over a particular operating range. The least squares method is used to minimise differences between the linear approximation and the full nonlinear mini-tab model (e.g. Figure 12). Figure 13 shows open and closed loop responses demonstrating LQR performance

using this linear reference model. The system is subject to an impulse excitation at an advance ratio of 1.17, just beyond the flutter boundary visible in Figure 14. It is important to note that while the LQR controller is designed with respect to linearised the mini-tab model, the stabilisation results represent the linear controller's performance when applied to the full nonlinear mini-tab model, with drag, and nonlinear aerodynamic loading included. The linear control design methods are shown to be sufficient despite the presence of nonlinearities.

Results are presented in Figure 14 for the damping improvement associated with mini-tab control across a range of advance ratios near the flutter stability boundary, covering $1.14 \leq V/\Omega R \leq 1.35$, where the plunge and surge modes' damping is critical. It was found that these modes undergo satisfactory damping improvement throughout this range.

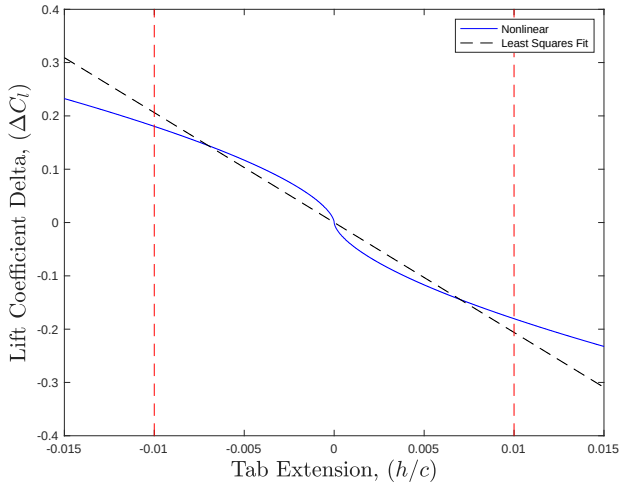

Figure 12: Least-squares fit to nonlinear mini-tab model for $\mathbf{h/c = \pm 0.01}$

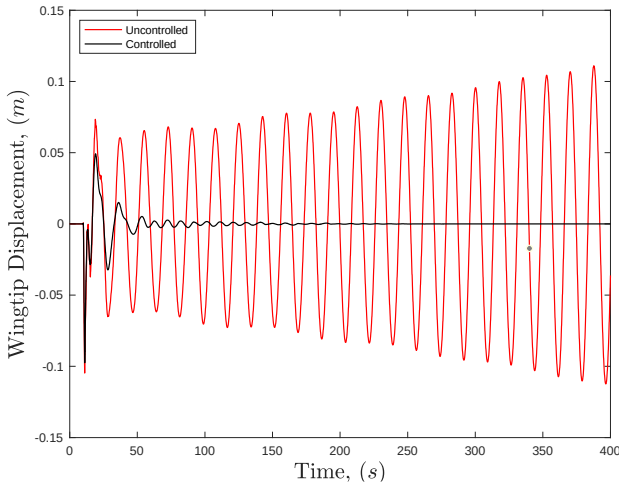

Figure 13: Improvement in response for the active (controlled) vs passive (uncontrolled) system at an advance ratio above the passive stability boundary.

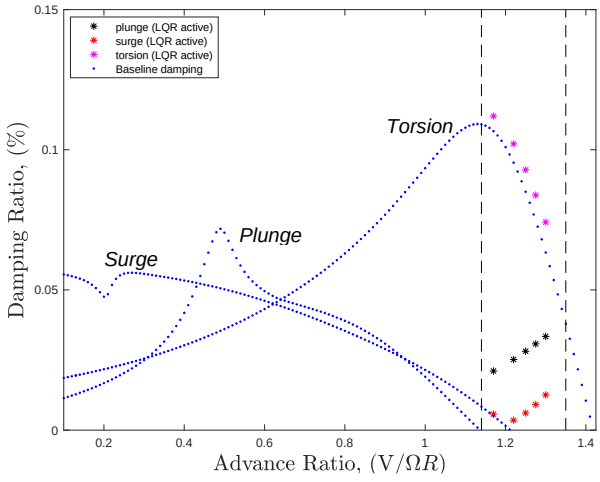

Figure 14: Mini-tab control damping improvement for $\mathbf{1.14 \leq V/\Omega R \leq 1.35}$

In general, the developed simulation architecture at this stage is deemed ready for integration with the experimental work. The linear control methods considered here offer a feasible means of implementing active mini-tab control and results to date suggest sufficient damping of modes critical for the XV-15 operation in cruise.

3.4. Future work

Experimental and simulation work to follow will be mutually beneficial. In the short-term, wind tunnel testing will contribute towards an updated unsteady aerodynamics model for the wing and a thorough characterisation of the mini-tab lift, pitching moment and drag variation with tab extension h/c and angle of attack. An updated nonlinear mini-tab model will be created based on the new, high-fidelity mini-tab data. The updated simulation results will then be validated experimentally to demonstrate the application of the methods.

Improvements to the numerical model will also be used in further simulation analysis aimed at providing detailed numerical quantification of the benefits to be expected from active mini-tab control including:

- **Maximum flutter boundary increase**: LQR weighting matrices will be tuned to maximise the flutter boundary increase for the XV-15 model. Realistic mini-tab constraints refined through tests on the current mini-tab rig, will inform the acceptable tab inputs suggested by digital simulation. This will allow for the determination of realistic flutter boundary increases.
- **Drag modelling penalty**: Assessment of the control penalty associated with using linear control on the nonlinear mini-tab system will

be made through comparison of LQR performance on linear mini-tab models relative to the performance on the full nonlinear model.

- **Measurement limitations**: Since realistic implementation of active mini-tab technology is unlikely to feature full-state sensor measurements, the influence of limitations in state measurements is of particular interest for practical feasibility assessment. This will be achieved through LQG analysis, with a Kalman filter estimation of non-measured states. The ultimate aim is to conduct hardware-in-the loop simulations whereby the developed LQG control may be applied to a physical mini-tab/wing system.

3.5. Conclusions

This paper discusses groundwork laid for the foundation of a novel investigation into the whirl flutter phenomenon and the efficacy of active mini-tab control. The design of a state of the art, experimental rig is outlined featuring a wing based on the XV-15 NACA 64A-223 profile and an embedded trailing edge mini-tab. This rig is shown to be capable of producing dynamic wing motions representative of whirl flutter experienced by the XV-15 tiltrotor in cruise.

Development of a low-order numerical whirl flutter model is presented, suitable for control development applications, and based on validated linear modelling approaches. Wing dynamics are included through classical finite element techniques and aerodynamics for the wing and rotor are included using quasi-steady strip theory and blade element theory respectively. Nonlinear mini-tab load models were included using empirical results from previous work at the University of Bath. Results show that the linear LQR controller is capable of stabilising the nonlinear system beyond the flutter boundary of the passive system, and that satisfactory increase in both plunge and surge mode damping is possible even with the necessity of neglecting drag forces in the linear control design approach.

Looking ahead, experimental and simulation work will be integrated closely. Wind tunnel tests scheduled for the immediate future will improve the current mini-tab and aerodynamic models available for simulation. Results from the improved models will inform test cases for experimental validation of the feasibility.

Longer term, the facilities described will permit full coupling of the numerical and experimental domains in hardware-in-the-loop tests as a further step towards a full technology demonstration.

The results presented show the feasibility of the mini-tab as an effective active load control device for improving whirl flutter stability boundaries, and showcase the steps taken towards experimental validation of the methods.

ACKNOWLEDGEMENTS

This work is supported by the EPSRC through the MENtOR project (EP/S011382/1) and conducted as part of the work of the UK VLN.

RERFERENCES

[1] Hathaway, E. L., and Gandhi, F., “Tiltrotor Whirl Flutter Alleviation Using Actively Controlled Wing Flaperons,” AIAA Journal, Vol. 44, No. 11, 2006, pp. 2524-2534. https://doi.org/10.2514/1.18428

[2] Acree, C., W., Peyran, R., J., and Johnson, W., “Rotor Design Options for Improving XV-15 Whirl-Flutter Stability Margins”, NASA/TP-2004-212262, 2004.

[3] Heathcote, D., Gursul, I., and Cleaver, D.J., “Dynamic Deployment of a Mini-tab for Aerodynamic Load Control”, Journal of Aircraft, Vol. 57, No. 1, January–February 2020, pp. 41-61.https://doi.org/10.2514/1.C035556

[4] Bull, S. C., “Unsteady Aerodynamics of Wings in Extreme Conditions”. Ph.D. Dissertation, Department of Mechanical Engineering, The University of Bath, Bath, England, U.K., 2020.

[5] Theodorsen, T., "General Theory of Aerodynamic Instability and the Mechanics of Flutter," NACA Technical Report, No. 496, NACA, 1949.

[6] Greenberg, J. M.1947 Airfoil in sinusoidal motion in a pulsating stream. NACA Technical Report, 1326.

[7] Brunton, S. L., Dawson, S. T. M., Rowley, W. C., “State-space model identification and feedback control of unsteady aerodynamic forces”. Journal of Fluids and Structures, Vol. 50, 2014, pp. 253-270. https://doi.org/10.1016/j.jfluidstructs.2014.06.026

[8] Johnson, W., "Development of a comprehensive analysis for rotorcraft. II-Aircraft model, solution procedure and applications.", NASA Ames Research Center; U.S. Army, Aeromechanics Laboratory, Moffett Field CA, United States, 1981.

[9] Bauchau, O.A., "DYMORE user’s manual.", Georgia Institute of Technology, Atlanta, 2007.

[10] Maisel, M.D., “The history of the XV-15 tilt rotor research aircraft: from concept to flight.”, No. 17. National Aeronautics and Space Administration, Office of Policy and Plans, NASA History Division, 2000.

[11] Johnson, W., “Dynamics of a tilting proprotor aircraft in cruise flight”. NASA Technical Note, NASA TN D-7677, 1974.

[12] Paik, J. et al., "Active tiltrotor whirl-flutter stability augmentation using wing-flaperon and swash-plate actuation.", Journal of aircraft, 44(5), pp. 1439-1446, 2007. http://dx.doi.org/10.2514/1.20234

[13] Nixon, M.W., "Aeroelastic response and stability of tiltrotors with elastically-coupled composite rotor blades." Ph.D. Dissertation, University of Maryland, College Park, 1993.

[14] Mair, C.; Titurus, B.; and Rezgui, D., "Stability analysis of whirl flutter in rotor-nacelle systems with freeplay nonlinearity.", Nonlinear Dynamics 104, no. 1, pp. 65-89, 2021. https://doi.org/10.1007/s11071-021-06271-z

[15] Zhaohua, F., and Cook, R.D. "Beam elements on two-parameter elastic foundations.", Journal of Engineering Mechanics, 109(6), pp. 1390-1402, 1983. https://doi.org/10.1061/(ASCE)0733-9399(1983)109:6(1390)

[16] Heathcote, D.J. et al., "Aerodynamic load alleviation using minitabs." Journal of Aircraft, 55(5), pp. 2068-2077, 2018. https://doi.org/10.2514/1.C034574